Robust integrated control/structure co-design for stratospheric balloons

Ervan Kassarian, Francesco Sanfedino, Daniel Alazard, Johan Montel, Charles-Antoine Chevrier

Available online at www.sciencedirect.com

ScienceDirect

IFAC PapersOnLine CONFERENCE PAPER ARCHIVE

IFAC PapersOnLine 55-25 (2022) 13–18

Robust integrated control/structure co-design for stratospheric balloons

E. Kassarian * **F. Sanfedino** * **D. Alazard** * **J. Montel** ** **C.A. Chevrier** **

* *ISAE-Supaero, Université de Toulouse, France (e-mail: ervan.kassarian@isae.fr).*

** *Centre National d'Etudes Spatiales (CNES), Toulouse, France*

Abstract: Stratospheric balloons offer cost-effective platforms for optical payloads in the context of astronomy missions. During the 2018 flight of the Faint Intergalactic medium Redshifted Emission Balloon (FIREBall) experiment, the moon light was scattered from the surface of the balloon and re-directed into the telescope which resulted in degraded optical performance. To reduce this parasite effect, it is sought to increase the length of the flight train. However, this change in the mechanical design significantly modifies the dynamics of the system and the pointing performance must not be altered. In this purpose, a robust integrated control/structure co-design method is proposed. After deriving a Linear Fractional Transformation (LFT) model of the system, the co-design is tackled as a multi-objective, structured, robust $\mathcal{H}_2/\mathcal{H}_\infty$ problem that is solved with a non-smooth optimization algorithm to maximize the train's length under constraints of pointing performance. By optimizing in a single iteration the controllers along with the structural parameter with regard to the worst-case configurations of the uncertain parameters, time-consuming procedures requiring not only to iterate between control and mechanical design, but also to analyze the robustness based on Monte-Carlo simulations, are avoided.

Keywords: Robust control, Integrated control/structure co-design, $\mathcal{H}_\infty$ control, Stratospheric balloons, Line-of-sight pointing control, LFT modeling

1. INTRODUCTION

Stratospheric balloons can transport optical instruments in the near-space environment for short-duration astronomy missions. Compared to propellant-based vehicles, their advantages include a much lower cost, the ability to carry and recover heavy payloads, short preparation times due to imposing few mechanical vibrations to the payload, and a high flexibility in the launching site and flight operations (Yajima et al., 2009, chap.1.3). Typical precision requirements are around the arcsecond Montel et al. (2019), and new missions start relying on fast-steering mirrors to reach precisions around the milli-arcsecond (Howe et al. (2017)). Developing accurate dynamical models and adequate control strategies is necessary to meet the growing need in pointing precision.

A dynamical model of balloon-borne flight chains, based on Lagrangian mechanics, was proposed in Kassarian et al. (2021). This model accounts for the pendulum-like oscillations of the system in the vertical planes, as well as the torsion of the filar suspensions around the vertical axis. The predictions of the model showed good agreement with flight data, and enabled stability analysis and control design. However, the Lagrangian approach is not suited for the representation of parametric uncertainties, such as the balloon's characteristics or the mass of ballast, which is released during the flight. Therefore, a Linear Fractional Transformation (LFT) model was developed in Kassarian et al. (2022b) and was applied to the Faint Intergalactic medium Redshifted Emission Balloon (FIREBall), a joint NASA/CNES experiment, to perform robust pointing control of the line-of-sight with $\mathcal{H}_\infty$-synthesis. In addition to the uncertain parameters, the LFT framework also allows to isolate structural parameters considered as decision variables, which brings to the focus of this paper.

Indeed, previous flight experience has shown that the moon light scattered from the surface of the balloon degraded the optical performance of the FIREBall instrument (Hamden et al. (2020); Picouet et al. (2020)). Therefore, it is discussed to increase the length of the flight train, in order to reduce the parasite light received by the instrument from the balloon, and the primary concern is the impact of such a design change on the pointing performance. However, not only is it possible to quantify this impact during the early design phase using the models developed in the aforementioned work, but the optimization of this length can also be addressed simultaneously with the controller design to ensure the closed-loop performance. Optimizing structural parameters along with the controller is generally referred to as integrated control/structure co-design. This multidisciplinary optimization effort comes from the increased complexity in structure/control interaction when lightweight and flexible structures have to cope with fine pointing requirements. By treating the structural parameters with the LFT frame-

⋆ This work was funded by ISAE-Supaero and CNES.

10.1016/j.ifacol.2022.09.316

work, it is possible to adopt a monolithic architecture, where a single optimization problem is solved, and which is generally more cost-efficient than distributed architectures where the same problem is divided into multiple coupled subproblems (Martins and Lambe (2013)). Moreover, LFT-based co-design approaches are also able to account for parametric uncertainties in the synthesis to bypass time-consuming simulation-based approaches like Monte-Carlo campaigns by directly optimizing the controller and the structure with regard to worst-case parametric configurations. Previous applications include, for example, the optimization of avionics parameters (Alazard et al. (2013)) or the maximization of the payload mass (Perez et al. (2016)) for large flexible space structure.

In this paper, a robust integrated control/structure co-design methodology is proposed to maximize the flight train's length of the stratospheric balloon FIREBall, presented in Section 2, to tackle the degradation of the optical performance observed in flight while ensuring robust pointing control of the line-of-sight. The LFT model of the system is derived in Section 3 using a multibody approach introduced in Kassarian et al. (2022a) to account for parametric uncertainties and variations of the length. In Section 4, it is shown that the length of the flight train has a complex impact on the dynamics of the system, and particularly on the flexible modes, which justifies the co-design approach. The control architecture is presented in Section 5. Finally, using modern non-smooth optimization methods (Apkarian and Noll (2006); Apkarian et al. (2015)), the optimization of the flight train's length along with the controller synthesis is addressed as a multi-objective, structured, robust $\mathcal{H}_2/\mathcal{H}_\infty$ problem in Section 6.

2. THE FIREBALL STRATOSPHERIC BALLOON

The FIREBall system is represented in Fig. 1. It is composed of a balloon, an un-deployed parachute discretized in four elements to account for its flexibility, a bi-filar suspension represented in red whose length L can be adjusted before the flight, several rigid bodies, and the platform, carrying up to 500 kg of ballast and the pointing system. The azimuth of the platform (angle around the vertical axis $\mathbf{z}$) is controlled, using a motorized pivot, so as to follow the sideral motion of the target. Additionally, two reaction wheels are able to provide torque to the platform to slightly damp the oscillations around $\mathbf{x}$- and $\mathbf{y}$-axes. The light arriving to the platform is reflected on a siderostat mirror, and then focused by a parabolic mirror to the instrument.

During the flight, the balloon is subject to wind disturbances that cause the platform to oscillate with an amplitude up to 0.15° around $\mathbf{x}$ and $\mathbf{y}$ axes, and the azimuth control leaves an error up to 0.005° around $\mathbf{z}$ (Montel et al. (2019)). The pointing system must compensate the motion of the platform to reach a line-of-sight pointing accuracy below the arc-second. For this purpose, the siderostat mirror is mounted on a gimbal and can be controlled around two axes called elevation and cross-elevation. The instrument is mounted on a rotating stage and controlled around a third axis called field rotation.

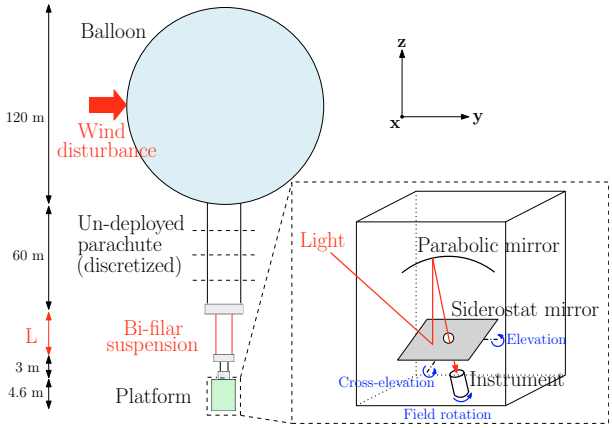

Fig. 1. The FIREBall stratospheric balloon

3. LFT MODELING OF THE SYSTEM

A general model of balloon-borne flight chains, relying on Lagrangian mechanics and small angles assumption, was proposed in Kassarian et al. (2021). Two types of dynamics are distinguished: (i) the pendulum-like oscillations of the elements of the flight chain around $\mathbf{x}$ and $\mathbf{y}$, triggered by wind disturbances, and (ii) the torsion of the suspensions around $\mathbf{z}$, triggered by both the natural rotation of the balloon and the control of the platform around $\mathbf{z}$. Although this model is satisfying in the nominal configuration, it is not suited to extract the train's length L as a design parameter to be tuned, or to take into account parametric uncertainties, such as the balloon's mechanical characteristics or the ballast mass that decreases from 500 kg to 0 during the flight.

To perform a robust control/structure co-design, it is necessary to derive a Linear Fractional Transformation (LFT) model of the system. A general method was developed in Kassarian et al. (2022a) to compute LFT models of multibody structures for any trim conditions. Each substructure is modeled independently from the others in the TITOP framework (Alazard et al. (2008, 2015)) with Newton-Euler equations to express the relationship between its motion and the wrench (force and torque) applied to it, and its parametric uncertainties are represented with an unknown, bounded operator $\mathbf{\Delta}$ allowing to isolate them from the nominal model with the LFT representation. Time-varying and design parameters are isolated using the LFT representation as well. The individual models are then assembled to directly obtain the LFT model of the structure, covering all parametric configurations in a single model.

The multibody LFT model of FIREBall is represented in Fig. 2. It is composed of rigid bodies $\mathcal{B}_i$, including for example the balloon, the platform and the siderostat mirror; suspensions $\mathcal{S}_i$ that have an additional degree of freedom (with regard to a rigid body) corresponding to their torsion around $\mathbf{z}$, including for example the discretized parachute and the adjustable bi-filar suspension; and joints $\mathcal{J}_i$ that allow the rotations around $\mathbf{x}$, $\mathbf{y}$ and/or $\mathbf{z}$. The green blocks represent the nominal models, the blue blocks represent parametric uncertainties, and the red block $\mathbf{\Delta}_L$ represents the variations of the structural parameter L considered for the control/structure co-design. The output $\delta\mathbf{m}_O^{\mathcal{B}_1} \in \mathbb{R}^{18}$ is

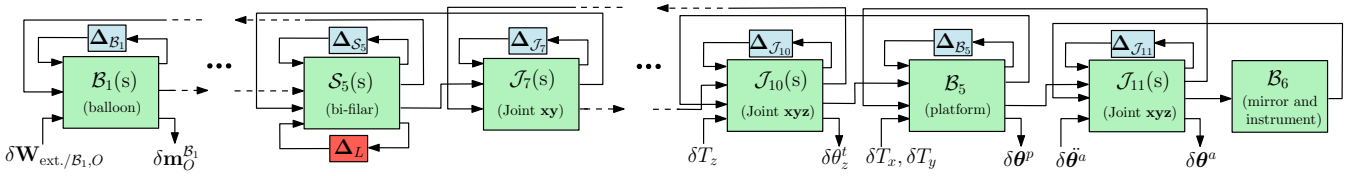

Fig. 2. Multibody LFT model of the system

the motion vector, containing the linear and angular accelerations, speeds and positions of the balloon $\mathbf{B}_1$ at point O. The input $\delta\mathbf{W}_{\text{ext}/\mathcal{B}_1,O} \in \mathbb{R}^6$ is the external wrench applied to $\mathcal{B}_1$ at point O. It includes the wind disturbances, the aerodynamic damping on the balloon's rotation (added as a feedback on the rotation rates of the balloon), and the variations of the buoyancy force projected in the reference frame attached to the balloon (added as feedback on the angular position of the balloon). The interconnection signals represent the wrenches applied from one body to another, and the motion vectors at connection points; they are not detailed for readability (the reader is referred to Kassarian et al. (2022a) for an exhaustive understanding). The joint $\mathcal{J}_{10}$ is actuated with a torque δT_z around $\mathbf{z}$ for azimuth control, and torques δT_x and δT_y can be applied to the gondola with reaction wheels for active damping. The output vector $\delta\boldsymbol{\theta}^p = \left[\,\delta\theta_x^p \;\; \delta\theta_y^p \;\; \delta\theta_y^p\,\right]^T$ contains the angles of the platform, and the scalar output $\delta\theta_z^t$ is the flight train's angle around $\mathbf{z}$. The angular positions of the actuators controlling the mirror and instrument in elevation, cross-elevation and field rotation respectively are regrouped in the vector $\delta\boldsymbol{\theta}^a = \left[\,\delta\theta_{\text{el}}^a \;\; \delta\theta_{\text{ce}}^a \;\; \delta\theta_{\text{fr}}^a\,\right]^T$.

4. INFLUENCE OF THE STRUCTURAL PARAMETER L ON THE DYNAMICS

The structural parameter L (length of the bi-filar suspension), considered for the control/structure co-design, has a significant impact on the dynamics of the system. The open-loop response of the platform to wind disturbances is shown in Fig. 3 for L varying between 10 m and 60 m. The resonances, which correspond to the first pendulum modes of the flight chain, are the main contributors to the motion of the platform, as it was observed in flight in the initial configuration L=21 m (Montel et al. (2019)). In particular, small values of L decrease the resonance peaks of the pendulum modes 3 and 4, but they move toward higher frequencies which are more difficult to reject by the pointing control of the line-of-sight inside the platform. Moreover, small values of L also increase the resonance peak of mode 2 and bring it to higher frequencies.

In other terms, the modal frequencies and dampings depend on L, as illustrated in Fig. 4a. The modal shapes also depend on L, as represented in Fig. 4b for the pendulum mode 4.

Finally, although it is not represented here, this dependency of the dynamics on L is also coupled with the parametric uncertainties. All these observations justify the need for a robust integrated control/structure co-design approach, since it is not easy to determine whether changing the mechanical design of the system will degrade the pointing performance.

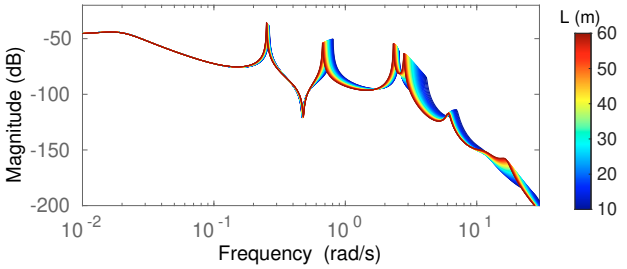

Fig. 3. Transfer from the wind disturbance to the platform's angle θ_x depending on L (nominal model)

5. CONTROL ARCHITECTURE

5.1 Primary control of the platform

The azimuth control is performed with a motorized pivot, which applies a torque δT_z to the gondola and the opposite torque $-\delta T_z$ to the bottom of the flight chain. The torque is computed with two controllers C_1 and C_2 using the reference azimuth δr^{az}, the platform's angle $\delta\theta_z^p$ and the flight train's angle $\delta\theta_z^t$, so as to ensure the tracking of the sideral motion of the science target by the platform, while damping the torsion modes of the flight train:

$$\delta T_z = C_1(\mathrm{s})\underbrace{\left(\delta r^{az} - \delta\hat{\theta}_z^p\right)}_{\delta e^{\text{az}}} + C_2(\mathrm{s})\delta\hat{\theta}_z^t \tag{1}$$

where δe^{az} is the azimuth error, with the estimated angles

$$\begin{cases} \delta\hat{\theta}_z^p = d_1(\mathrm{s})\delta\theta_z^p \\ \delta\hat{\theta}_z^t = d_1(\mathrm{s})\left(\frac{40\mathrm{s}}{40\mathrm{s}+1}\right)^2\delta\theta_z^t \end{cases} \tag{2}$$

where $d_1(\mathrm{s})$ designates a third-order Padé approximation of a 70 ms delay of the numerical gyrometer, and a low-pass filter is applied to the flight train's angle $\delta\theta_z^t$ to avoid low-frequency drift. The dynamics of the motorized pivot are considered fast enough and the measurement noise small enough to be neglected.

Additionally, two reaction wheels are mounted on the platform and are able to provide small torques around $\mathbf{x}$ and $\mathbf{y}$ respectively. They are characterized by the transfer function $\mathbf{A}^{\text{w}}$ between the torques δT_x and δT_y and the voltages δV_x and δV_y respectively:

$$\begin{bmatrix}\delta T_x \\ \delta T_y\end{bmatrix} = \mathbf{A}^{\text{w}}(\mathrm{s})\begin{bmatrix}\delta V_x \\ \delta V_y\end{bmatrix} \tag{3}$$

and the voltages are computed proportional to the platform's rotation rates with the controller C_3:

$$\begin{bmatrix}\delta V_x \\ \delta V_y\end{bmatrix} = -C_3(\mathrm{s})\begin{bmatrix}\delta\hat{\dot{\theta}}_x^p \\ \delta\hat{\dot{\theta}}_y^p\end{bmatrix} \tag{4}$$

with the estimated rotation rates

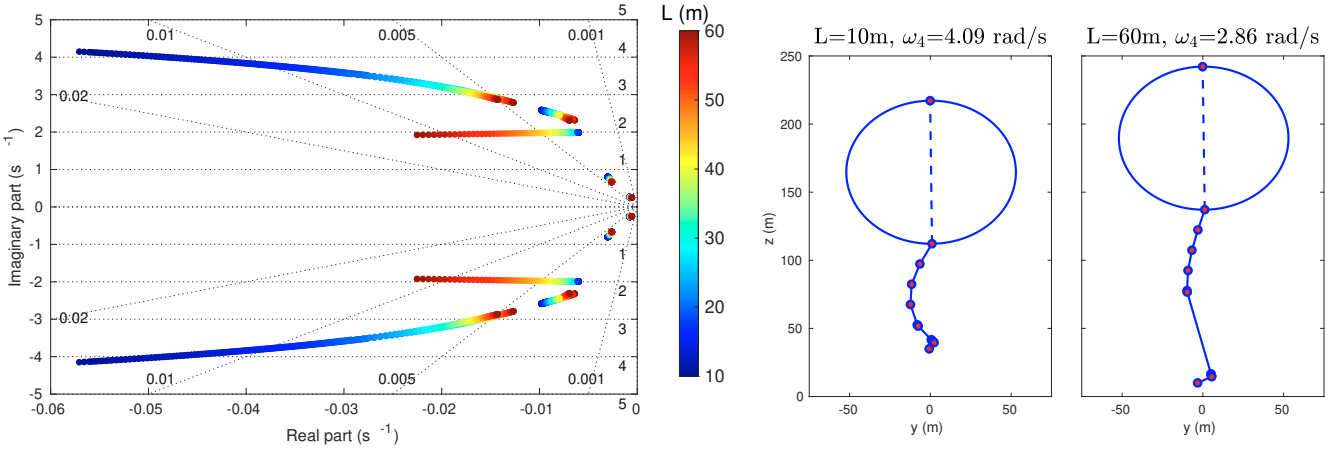

(a) Root locus depending on L (first modes)

(b) Pendulum mode 4, **x**-axis: modal shape for 2 values of L

Fig. 4. Eigenmodes of the system, depending on the length L of the bi-filar suspension (nominal model)

$$\begin{cases} \delta\hat{\dot{\theta}}^p_x = d_1(\mathrm{s})\delta\dot{\theta}^p_x \\ \delta\hat{\dot{\theta}}^p_y = d_1(\mathrm{s})\delta\dot{\theta}^p_y \end{cases} \tag{5}$$

to provide a small active damping to the pendulum modes of the flight chain. Measurement noise is neglected.

5.2 Line-of-sight pointing control

The line-of-sight (LOS) is defined with three successive rotations imposed by the actuators, namely elevation, cross-elevation and field rotation, as represented in Fig. 1. The line-of-sight angles, expressed in elevation, cross-elevation and field rotation, are contained in the vector $\delta\boldsymbol{\theta}^{\mathrm{LOS}} = \left[\, \delta\theta^{\mathrm{LOS}}_{\mathrm{el}} \;\; \delta\theta^{\mathrm{LOS}}_{\mathrm{ce}} \;\; \delta\theta^{\mathrm{LOS}}_{\mathrm{fr}} \,\right]^T$ and depend on the platform's angles $\delta\boldsymbol{\theta}^p$ and the actuator's angles $\delta\boldsymbol{\theta}^a$ following the relation:

$$\delta\boldsymbol{\theta}^{\mathrm{LOS}} = \mathcal{F}_u(\mathbf{P}, \boldsymbol{\Delta}_{\mathrm{el}})\delta\boldsymbol{\theta}^p + \mathbf{R}\delta\boldsymbol{\theta}^a \tag{6}$$

where $\mathbf{R} = \mathrm{diag}(2, 2, 1)$ accounts for the reflections on the elevation and cross-elevation axes, $\mathcal{F}_u(.)$ designates the upper LFT, the operator $\boldsymbol{\Delta}_{\mathrm{el}}$ expresses the variations of the equilibrium elevation angle, and $\mathcal{F}_u(\mathbf{P}, \boldsymbol{\Delta}_{\mathrm{el}})$ accounts for the rotations between the platform and the line-of-sight. It should be noted that, with this definition, the action of the actuators is decoupled on the three angles of the LOS.

The instrument is equipped with an optical guider that directly measures the line-of-sight:

$$\delta\hat{\boldsymbol{\theta}}^{\mathrm{LOS}}_{\mathrm{optic}} = d_2(\mathrm{s})\delta\boldsymbol{\theta}^{\mathrm{LOS}} + \mathbf{n}_{\mathrm{guider}} \tag{7}$$

where $d_2(\mathrm{s})$ designates a third-order Padé approximation of a 40 ms delay, and $\mathbf{n}_{\mathrm{guider}}$ is the measurement noise of the guider. Furthermore, the line-of-sight is estimated with equation (6) from the measurements of the platform's rotation rates with an analogical gyrometer and of the actuator's angular positions:

$$\delta\hat{\boldsymbol{\theta}}^{\mathrm{LOS}}_{\mathrm{gyro}} = \mathcal{F}_u(\mathbf{P}, \boldsymbol{\Delta}_{\mathrm{el}})\frac{1}{\mathrm{s}}(\delta\dot{\boldsymbol{\theta}}^p + \mathbf{n}_{\mathrm{gyro}}) + \mathbf{R}d_3(\mathrm{s})\delta\boldsymbol{\theta}^a \tag{8}$$

where $d_3(\mathrm{s})$ designates a third-order Padé approximation of a 1 ms delay, and $\mathbf{n}_{\mathrm{gyro}}$ is the measurement noise of the gyrometer. The delay of the gyrometer's and the noise of the actuators' measurements are negligible. The estimate $\delta\hat{\boldsymbol{\theta}}^{\mathrm{LOS}}_{\mathrm{optic}}$ (equation (7)) has a larger delay, but $\delta\hat{\boldsymbol{\theta}}^{\mathrm{LOS}}_{\mathrm{gyro}}$ (equation (8)) has higher noise ; therefore, both are filtered to provide a better estimate $\delta\hat{\boldsymbol{\theta}}^{\mathrm{LOS}}$:

$$\delta\hat{\boldsymbol{\theta}}^{\mathrm{LOS}} = (\mathbf{I}_3 - \mathbf{F}(\tau_1, \tau_2, \mathrm{s}))\,\delta\hat{\boldsymbol{\theta}}^{\mathrm{LOS}}_{\mathrm{optic}} + \mathbf{F}(\tau_1, \tau_2, \mathrm{s})\delta\hat{\boldsymbol{\theta}}^{\mathrm{LOS}}_{\mathrm{gyro}} \tag{9}$$

where the filter $\mathbf{F}(\tau_1, \tau_2, \mathrm{s})$ is expressed as the lower LFT:

$$\mathbf{F}(\tau_1, \tau_2, \mathrm{s}) = \frac{\tau_1\mathrm{s}}{\tau_1\mathrm{s}+1}\frac{\tau_2\mathrm{s}}{\tau_2\mathrm{s}+1}\mathbf{I}_3 = \mathcal{F}_l\left(\mathbf{F}(\mathrm{s}), \left[\begin{smallmatrix} \tau_1\mathbf{I}_3 & \mathbf{0} \\ \mathbf{0} & \tau_2\mathbf{I}_3 \end{smallmatrix}\right]\right) \tag{10}$$

and the parameters τ_1 and τ_2 are tuned during the controller synthesis.

Finally, the actuators in elevation, cross-elevation and field rotation are characterized by their transfer functions A_{el}, A_{ce}, A_{fr} between the voltages δV_{el}, δV_{ce}, δV_{fr} and the angular accelerations $\delta\ddot{\theta}^a_{\mathrm{el}}$, $\delta\ddot{\theta}^a_{\mathrm{ce}}$, $\delta\ddot{\theta}^a_{\mathrm{fr}}$ respectively:

$$\begin{cases} \delta\ddot{\theta}^a_{\mathrm{el}} = A_{\mathrm{el}}(\mathrm{s})\delta V_{\mathrm{el}} \\ \delta\ddot{\theta}^a_{\mathrm{ce}} = A_{\mathrm{ce}}(\mathrm{s})\delta V_{\mathrm{ce}} \\ \delta\ddot{\theta}^a_{\mathrm{fr}} = A_{\mathrm{fr}}(\mathrm{s})\delta V_{\mathrm{fr}} \end{cases} \tag{11}$$

and the voltages are computed with the controllers K_{el},K_{ce},K_{fr} and the reference angles $\delta r^{\mathrm{LOS}}_{\mathrm{el}}$,$\delta r^{\mathrm{LOS}}_{\mathrm{ce}}$,$\delta r^{\mathrm{LOS}}_{\mathrm{fr}}$:

$$\begin{cases} \delta V_{\mathrm{el}} = K_{\mathrm{el}}(\mathrm{s})(\delta r^{\mathrm{LOS}}_{\mathrm{el}} - \delta\hat{\theta}^{\mathrm{LOS}}_{\mathrm{el}}) \\ \delta V_{\mathrm{ce}} = K_{\mathrm{ce}}(\mathrm{s})(\delta r^{\mathrm{LOS}}_{\mathrm{ce}} - \delta\hat{\theta}^{\mathrm{LOS}}_{\mathrm{ce}}) \\ \delta V_{\mathrm{fr}} = K_{\mathrm{fr}}(\mathrm{s})(\delta r^{\mathrm{LOS}}_{\mathrm{fr}} - \delta\hat{\theta}^{\mathrm{LOS}}_{\mathrm{fr}}) \end{cases} \tag{12}$$

also written, with $\delta\mathbf{e}^{\mathrm{LOS}}$ the 3-axes pointing error, as:

$$\delta\mathbf{V} = \mathrm{diag}(K_{\mathrm{el}}, K_{\mathrm{ce}}, K_{\mathrm{fr}})\underbrace{(\delta\mathbf{r}^{\mathrm{LOS}} - \delta\hat{\boldsymbol{\theta}}^{\mathrm{LOS}})}_{\delta\mathbf{e}^{\mathrm{LOS}}}. \tag{13}$$

6. CONTROL/STRUCTURE CO-DESIGN

6.1 Closed-loop system

The closed-loop model is presented in Fig. 5:

- The green blocks represent the nominal models: $\mathbf{M}(\mathrm{s})$ includes the model presented in Section 3 and the models of actuators and delays presented in Section 5, and $\mathbf{E}(\mathrm{s})$ represents the line-of-sight estimation,
- The blue blocks $\boldsymbol{\Delta}_M$ and $\boldsymbol{\Delta}_E$ regroup the parametric uncertainties on the mechanical system and estimation respectively,

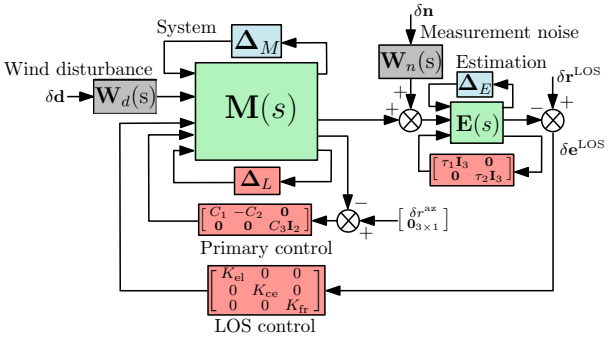

Fig. 5. Closed-loop block diagram

- The red blocks are the decision variables: length of the bifilar suspension with the block $\boldsymbol{\Delta}_L$; primary control with C_1, C_2 and C_3; estimation with τ_1 and τ_2; and line-of-sight pointing control with K_{el}, K_{ce} and K_{fr},
- The grey blocks $\mathbf{W}_d$ and $\mathbf{W}_n$ model the frequency content of the wind disturbance and of the measurement noise respectively,
- The input $\delta\mathbf{d} \in \mathbb{R}^2$ regroups the normalized wind disturbances (forces) applied to the balloon along $\mathbf{x}$ and $\mathbf{y}$,
- The input $\delta\mathbf{n} \in \mathbb{R}^6$ regroups the normalized measurement noises of the guider and gyrometer.

Let us note $\boldsymbol{\Delta} = \text{diag}(\boldsymbol{\Delta}_M, \boldsymbol{\Delta}_E)$ the set of uncertainties. The matrices $\boldsymbol{\Delta}$ and $\boldsymbol{\Delta}_L$ are squared, diagonal, with a size of 130 and 18 respectively. The controllers C_1, C_2, C_3 are chosen of 2nd-order, and K_{el}, K_{ce}, K_{fr} of 3-rd order, as it was found to yield satisfying performance against a reasonable complexity.

6.2 Performance requirements

The control requirements are expressed as the constraints (14) to (21) that must be verified in closed-loop for any configuration of the uncertain parameters.

Active damping

Limitation of the reaction wheel voltage variance:

$$\max_{\boldsymbol{\Delta}} \left\{ || \ \delta\mathbf{d} \to \mathbf{W}_1 \begin{bmatrix} \delta V_x \\ \delta V_y \end{bmatrix} \ ||_2 \right\} < \gamma_1 < 1 \tag{14}$$

Azimuth control

Reference tracking:

$$\max_{\boldsymbol{\Delta}} \{ || \ \delta r^{\text{az}} \to W_2 \delta e^{\text{az}} \ ||_\infty \} < \gamma_2 < 1 \tag{15}$$

Limitation of the torsion of the flight train:

$$\max_{\boldsymbol{\Delta}} \{ || \ \delta r^{\text{az}} \to W_3 \delta\theta_z^t \ ||_\infty \} < \gamma_3 < 1 \tag{16}$$

Limitation of the torque generated by the motorized pivot:

$$\max_{\boldsymbol{\Delta}} \{ || \ \delta r^{\text{az}} \to W_4 \delta T_z \ ||_\infty \} < \gamma_4 < 1 \tag{17}$$

Line-of-sight pointing control

Reference tracking:

$$\max_{\boldsymbol{\Delta}} \{ || \ \delta\mathbf{r}^{\text{LOS}} \to \mathbf{W}_5 \delta\mathbf{e}^{\text{LOS}} \ ||_\infty \} < \gamma_5 < 1 \tag{18}$$

Disturbance rejection:

$$\max_{\boldsymbol{\Delta}} \{ || \ \begin{bmatrix} \delta\mathbf{d} \\ \delta\mathbf{n} \end{bmatrix} \to \mathbf{W}_6 \delta\mathbf{e}^{\text{LOS}} \ ||_\infty \} < \gamma_6 < 1 \tag{19}$$

Limitation of the actuators' motion:

$$\max_{\boldsymbol{\Delta}} \{ || \ \begin{bmatrix} \delta\mathbf{d} \\ \delta\mathbf{n} \end{bmatrix} \to \mathbf{W}_7 \delta\boldsymbol{\theta}^a \ ||_\infty \} < \gamma_7 < 1 \tag{20}$$

Stable controllers:

$$\text{s is a pole of } \text{diag}(K_{\text{el}}, K_{\text{ce}}, K_{\text{fr}}) \implies \text{Re(s)} < 0 \tag{21}$$

The filters 1 to 4 impose a $1\,\text{rad}\,\text{s}^{-1}$ bandwidth to the primary pointing control while limiting the control efforts:

$$\begin{cases} \mathbf{W}_1 = 3\,\mathbf{I}_2 \\ W_2 = \frac{\text{s}^2+1.4\text{s}+1}{1.2(\text{s}^2+1.4\text{s})} \\ W_3 = 3.16 \times 10^{-3} \\ W_4 = 1.78 \times 10^{-4} \end{cases} . \tag{22}$$

The line-of-sight reference tracking requirement yields the filter $\mathbf{W}_5$ which penalizes low-frequency error:

$$\mathbf{W}_5 = \frac{1}{2}\text{diag}\left(\frac{\text{s}+20}{\text{s}+0.02}, \frac{\text{s}+20}{\text{s}+0.02}, \frac{\text{s}+5}{\text{s}+0.005} \right) . \tag{23}$$

Following the methodology presented in Ott et al. (2013), the pointing performance is defined as the relative pointing error (RPE) across a time window $t = 100\,\text{s}$:

$$\mathbf{W}_6 = \frac{t^2\text{s}^2 + t\sqrt{12}\text{s}}{t^2\text{s}^2 + 6t\text{s} + 12}\text{diag}(2\times10^6, 2\times10^6, 3.3\times10^4) . \tag{24}$$

Finally, the filter $\mathbf{W}_7$:

$$\mathbf{W}_7 = 2.5\times10^5 \times \frac{\text{s}^2 + 0.56\text{s} + 0.16}{\text{s}^2 + 56\text{s} + 1600}\left(\frac{100\text{s}+0.01}{100\text{s}+1}\right)^2 \mathbf{I}_3 \tag{25}$$

penalizes high-frequency solicitation of the actuators.

6.3 Synthesis

Let us note $\mathbf{D} = \{L, C_1, C_2, C_3, \tau_1, \tau_2, K_{\text{el}}, K_{\text{ce}}, K_{\text{fr}}\}$ the set of decision variables. To reduce the parasite light scattered from the balloon and received by the instrument it is sought to maximize the train's length L; the integrated control/structure co-design is formulated as the multi-objective, structured, robust $\mathcal{H}_2/H_\infty$ problem:

$$\begin{aligned} &\underset{\mathbf{D}}{\text{minimize:}} \quad 1/L \\ &\text{subject to: constraints (14) to (21)} \end{aligned} \tag{26}$$

which is solved with a non-smooth optimization algorithm based on Apkarian and Noll (2006) (MATLAB routine `systune`). The synthesis is initialized with the configuration presentend in Kassarian et al. (2022b), that is, with L=21 m and a set of controllers that respected the constraints (14) to (21). After optimization, the length $\hat{L}$=39 m is obtained. The performance indices are summarized in Table 1 for the initial and final design, and, for illustration, Fig. 6 presents the transfer corresponding to the disturbance rejection constraint (19), where the overall shape is due to the measurement noise and the sharp uncertain peaks are due to the flexible modes.

Table 1. Performance indices

	L (m)	γ_1	γ_2	γ_3	γ_4	γ_5	γ_6	γ_7
initial	21	1.0	0.94	0.94	0.66	0.86	0.89	0.72
final	39	0.55	0.95	0.98	0.98	0.98	0.80	1.0

The co-design has allowed to increase the train's length and to improve the RPE (index γ_6). However, the control efforts (indices γ_4 and γ_7) are significantly increased and

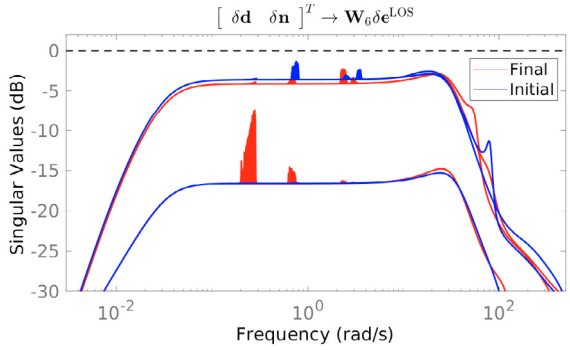

Fig. 6. Closed-loop transfer: disturbance rejection

pushed close to the performance limit. Finally, it should be noted that the synthesis requires a reasonable initialization of the decision variables, and that the pointing performance can most likely be further improved after settling the length and performing classical robust control design, for example seeking to minimize the RPE (performance index γ_6), as presented in Kassarian et al. (2022b).

7. CONCLUSION

A robust control/structure co-design approach was proposed for stratospheric balloons and applied to the Faint Intergalactic medium Redshifted Emission Balloon (FIREBall) experiment. An LFT model of the system was obtained with a multibody approach, and augmented with models of the actuators and sensors dynamics. Then, the length of the flight train was optimized along with the controllers under a set of constraints expressing the control requirements with regard to the worst-case configurations of parametric uncertainties. The main advantage of this approach is to avoid time-consuming iterative procedures, such as distributed co-design approaches or simulation-based robustness analysis like Monte-Carlo campaigns.

REFERENCES

Alazard, D., Loquen, T., Plinval, H.D., and Cumer, C. (2013). Avionics / Control co-design for large flexible space structures. In *AIAA Guidance, Navigation, and Control Conference*.

Alazard, D., Cumer, C., and Tantawi, K. (2008). Linear dynamic modeling of spacecraft with various flexible appendages and on-board angular momentums. *7th International ESA Conference on Guidance, Navigation and Control Systems*, 41(2), 11148–11153. doi: 10.3182/20080706-5-KR-1001.3581.

Alazard, D., Perez, J.A., Loquen, T., and Cumer, C. (2015). Two-input two-output port model for mechanical systems. In *AIAA Guidance, Navigation, and Control Conference, 2013*. American Institute of Aeronautics and Astronautics, Reston, Virginia. doi: 10.2514/6.2015-1778.

Apkarian, P., Dao, M.N., and Noll, D. (2015). Parametric Robust Structured Control Design. *IEEE Transactions on Automatic Control*, 60(7), 1857–1869. doi: 10.1109/TAC.2015.2396644.

Apkarian, P. and Noll, D. (2006). Nonsmooth H infinity synthesis. 51, 71–86.

Hamden, E., Martin, D.C., Milliard, B., Schiminovich, D., Nikzad, S., Evrard, J., Kyne, G., Grange, R., Montel, J., Pirot, E., Hoadley, K., O'sullivan, D., Melso, N., Picouet, V., Vibert, D., Balard, P., Blanchard, P., Crabill, M., Pascal, S., Mirc, F., Bray, N., Jewell, A., Blue Bird, J., Zorilla, J., Ong, H.R., Matuszewski, M., Lingner, N., Augustin, R., Limon, M., Gomes, A., Tapie, P., Soors, X., Zenone, I., and Saccoccio, M. (2020). FIREBall-2: The Faint Intergalactic Medium Redshifted Emission Balloon Telescope. *The Astrophysical Journal*, 898(2). doi:10.3847/1538-4357/aba1e0.

Howe, G.A., Mendillo, C.B., Hewawasam, K., Chakrabarti, S., Cook, T.A., Martel, J., and Finn, S.C. (2017). The low-order wavefront control system for the PICTURE-C mission: preliminary testbed results from the Shack-Hartmann sensor. *Proceedings of SPIE*. doi: 10.1117/12.2274122.

Kassarian, E., Sanfedino, F., Alazard, D., Evain, H., and Montel, J. (2021). Modeling and stability of balloon-borne gondolas with coupled pendulum-torsion dynamics. *Aerospace Science and Technology*, 112, 106607. doi: 10.1016/j.ast.2021.106607.

Kassarian, E., Sanfedino, F., Alazard, D., Chevrier, C.A., and Montel, J. (2022a). Linear fractional transformation modeling of multibody dynamics around parameter-dependent equilibrium. *IEEE Transactions on Control Systems Technology*, 1–8. doi: 10.1109/TCST.2022.3167610.

Kassarian, E., Sanfedino, F., Alazard, D., Montel, J., and Chevrier, C.A. (2022b). Robust line-of-sight pointing control on-board a stratospheric balloon-borne platform. *ArXiv e-prints*, 1–17.

Martins, J.R. and Lambe, A.B. (2013). Multidisciplinary design optimization: A survey of architectures. *AIAA Journal*, 51(9), 2049–2075. doi:10.2514/1.J051895.

Montel, J., Pérot, E., Mirc, F., Evrard, J., Melso, N., and Schiminovich, D. (2019). FIREBALL-2 (2018) in-flight pointing performance. In *24th ESA symposium on European rocket and balloon programmes and related research*, 51–57. ESA publications, Essen, Germany.

Ott, T., Fichter, W., Bennani, S., and Winkler, S. (2013). Precision pointing H infinity control design for absolute, window-, and stability-time errors. *CEAS Space Journal*, 4(1-4), 13–30. doi:10.1007/s12567-012-0028-z.

Perez, J.A., Pittet, C., Alazard, D., and Loquen, T. (2016). Integrated Control/Structure Design of a Large Space Structure using Structured Hinfinity Control. *IFAC-PapersOnLine*, 49(17), 302–307. doi: 10.1016/j.ifacol.2016.09.052.

Picouet, V., Milliard, B., Kyne, G., Vibert, D., Schiminovich, D., Martin, C., Hamden, E., Hoadley, K., Montel, J., Melso, N., O'Sullivan, D., Evrard, J., Perot, E., Grange, R., Nikzad, S., Balard, P., Blanchard, P., Mirc, F., Bray, N., Jewell, A., and Quiret, S. (2020). End-to-end ground calibration and in-flight performance of the FIREBall-2 instrument. *Journal of Astronomical Telescopes, Instruments, and Systems*, 6(04), 1–20. doi: 10.1117/1.jatis.6.4.044004.

Yajima, N., Imamura, T., Izutsu, N., and Abe, T. (2009). *Scientific ballooning: Technology and applications of exploration balloons floating in the stratosphere and the atmospheres of other planets*. Springer Science and Business Media. doi:10.1007/978-0-387-09727-5.